

A microscopic design rule for spin supersolids in triangular-lattice magnets

Ryota Ono,¹ Jun'ichi Ieda,¹ Michiyasu Mori,¹ and Sadamichi Maekawa^{1,2}

¹*Advanced Science Research Center, Japan Atomic Energy Agency,
2-4 Shirakata, Tokai-mura, Ibaraki, 319-1195, Japan*

²*RIKEN Center for Emergent Matter Science (CEMS), Wako 351-0198, Japan*

Spin supersolids emerge as a central topic in frustrated magnetism, motivating the search for realization in quantum materials. To this end, we study the origin of exchange anisotropy, Δ , in triangular-lattice cobaltate families $X_2Y\text{Co}(\text{PO}_4)_2$ and $X_2\text{Co}(\text{SeO}_3)_2$ ($X = \text{Na, K, Rb, Cs}$; $Y = \text{Mg, Ca, Sr, Ba}$) by tailoring realistic spin models. We show that Δ is determined by the ratio of trigonal crystal field to spin-orbit coupling strength. This framework explains contrasting anisotropies in these families, predicts systematic trends in Δ across X/Y -substitutions, and identifies candidate materials for spin supersolids. Our results establish trigonal field engineering as a microscopic route toward the design of spin supersolids.

Spin supersolids have attracted broad interest as an experimentally accessible realization of supersolidity in frustrated quantum magnets [1–9]. They represent a rare quantum phase in which crystalline order and phase-coherent transverse magnetism coexist, while also offering promising low-temperature functionalities such as enhanced magnetocaloric response [10] and potentially dissipationless spin transport [11–14]. Because their stability depends sensitively on exchange anisotropy, understanding the microscopic origin of anisotropy is central to the materials design of spin supersolids [15].

Recent experiments have reported signatures of a spin supersolid in $\text{Na}_2\text{BaCo}(\text{PO}_4)_2$ [10, 16] and $\text{K}_2\text{Co}(\text{SeO}_3)_2$ [17–19]. In addition, for the newly synthesized $\text{Rb}_2\text{Co}(\text{SeO}_3)_2$, recent studies contradict each other on the emergence of the spin supersolid [20, 21]. They are members of the $X_2Y\text{Co}(\text{PO}_4)_2$ (XYCP) and $X_2\text{Co}(\text{SeO}_3)_2$ (XCOS) families ($X = \text{Na, K, Rb, Cs}$, $Y = \text{Mg, Ca, Sr, Ba}$) [22–24], in which Co^{2+} in distorted CoO_6 octahedra hosts a spin-orbit-entangled Kramers doublet on a quasi-two-dimensional triangular-lattice. A widely used minimal model to describe these materials is the pseudospin-1/2 XXZ model on a triangular-lattice

$$\mathcal{H}_{\text{XXZ}} = \sum_{\langle ij \rangle} J \left[(e_i^x e_j^x + e_i^y e_j^y) + \Delta e_i^z e_j^z \right], \quad (1)$$

where $J > 0$ is the antiferromagnetic exchange parameter, $\mathbf{e}_i = (e_i^x, e_i^y, e_i^z)$ denotes the pseudospin-1/2 operator at site i , and Δ is the exchange anisotropy [25–27]. Theoretically, this model has been studied extensively as a function of Δ [9, 15, 25–27]. These studies establish that a supersolid is stabilized for $\Delta > 1$, while a superfluid is stabilized for $\Delta < 1$.

For materials design, however, one must identify which microscopic ingredient in the local electronic structure controls Δ . The issue is already evident experimentally: NaBaCP and KCSO have similar local CoO_6 coordination, yet their estimated anisotropies differ by almost an order of magnitude, $\Delta \simeq 1.7$ and $\Delta \simeq 14.3$, respectively [18, 28, 29]. This striking contrast raises a question: what local ingredient controls Δ , and can it be used

to chemically drive a transition between supersolid and superfluid?

In this Letter, starting from first-principles electronic structures and strong-coupling theory, we calculate anisotropic exchange parameters for the XYCP and XCOS families. We further establish a symmetry-based mapping from the local crystal field to Δ , providing a unified interpretation of our microscopic results. This mapping quantitatively captures the overall trend of Δ across Co^{2+} -based triangular-lattice antiferromagnets (TLAFs) and provides a concrete route toward materials design of spin supersolids.

NaBaCP and KCSO crystallize in the space groups $P\bar{3}m1$ [30, 31] and $R\bar{3}m$ [32], respectively [Fig. 1(a)]. In both cases, Co^{2+} having pseudospin-1/2 Kramers doublet [$J_{\text{eff}} = 1/2$ as shown in Fig. 1(b)] forms a quasi-two-dimensional triangular-lattice [Fig. 1(c)], implying inversion centers at the midpoints of all bonds. Moreover, the Co^{2+} site has local D_{3d} symmetry (threefold rotation with inversion). Hypothetical substituted members of the XYCP and XCOS families are generated by structural optimization starting from the parent NaBaCP and KCSO structures. These substitution provide a controlled way to tune the crystal field.

To study a relation between the crystal field and Δ , we construct a multi-orbital Hubbard model using electronic structures from first-principles calculations within generalized gradient approximation [33–35], in a spinor Wannier basis of five $\text{Co-}3d$ orbitals (ten spin-orbitals) obtained by the maximally localized Wannier-function method [36, 37]. The screened on-site Coulomb interaction is evaluated by constrained random-phase approximation [38] and is represented in the spherical Kanamori form (see Sec. S1 of Supplemental Material (SM) [35] for details of the electronic model). The resulting parameters and the detailed parametrization for XBaCP and XCOS are summarized in the Sec. S1 of SM [35]. The hopping integrals are found much smaller than the on-site Coulomb interaction, this justifies a strong-coupling superexchange treatment.

To extract realistic anisotropic exchange interactions,

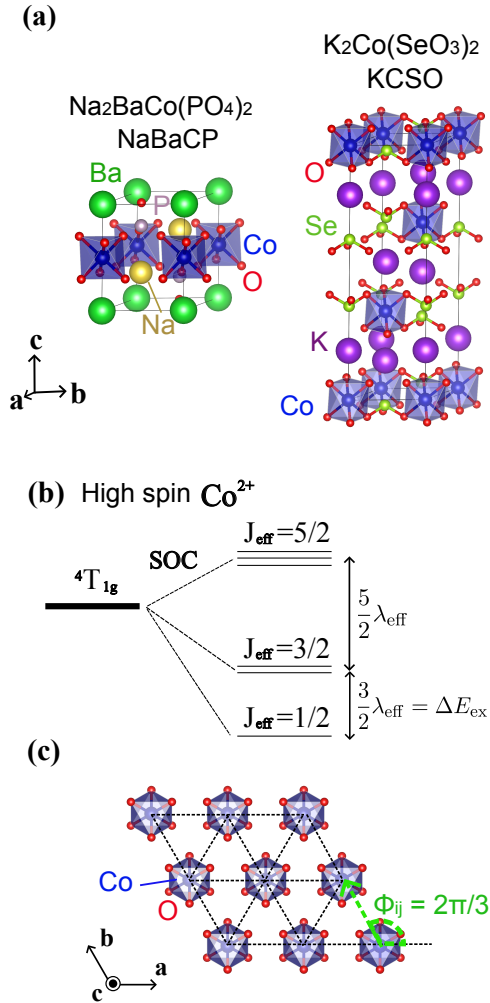


Figure 1. (a) Crystal structure of NaBaCP and KCSO. (b) Energy level scheme of the lowest multiplet of Co²⁺ in an octahedral crystal field with spin-orbit coupling (SOC). The energy gap between the $J_{\text{eff}} = 1/2$ ground state doublet and the first excited spin-orbit multiplet is denoted by ΔE_{ex} . (c) triangular-lattice plane formed by CoO₆ clusters in NaBaCP and KCSO. The green dashed arrow indicates the bond along the crystallographic **b**-axis ($\phi_{ij} = 2\pi/3$).

we perform a strong-coupling superexchange expansion of the Hubbard model [35, 39–43]. First, we obtain the local d^7 ground-state Kramers doublet $|\Psi^\pm\rangle$ on each Co²⁺ site. Then, the Kramers doublet wave-function projected on to the pseudospin direction, $\pm a$ ($a = x, y, z$), $|\varphi^{\pm a}\rangle$ is obtained as a linear combination $|\varphi^{\pm a}\rangle = c_{\pm}^{\pm a}|\Psi^+\rangle + c_{\pm}^{\mp a}|\Psi^-\rangle$, where $c_{\pm}^{\pm a}$ are linear combination coefficients of a Kramers doublet. Integrating out virtual charge fluctuations using this basis yield the second-order energy correction. For a two-site pseudospin wave-function $|\varphi_i^{\pm a}, \varphi_j^{\pm b}\rangle$, we have:

$$E_{ij}^{(2)}(\pm a, \pm b) = \langle \varphi_i^{\pm a}, \varphi_j^{\pm b} | \hat{T}_{ij} + \hat{T}_{ji} | \varphi_i^{\pm a}, \varphi_j^{\pm b} \rangle, \quad (2)$$

where \hat{T}_{ij} is the second-order perturbation operator asso-

ciated with virtual electron hopping processes from site j to i (see Sec. S2 of the SM for details of \hat{T}_{ij} [35]). From the four collinear configurations, the exchange tensor is obtained as $J_{ij}^{ab} = [E_{ij}^{(2)}(+a, +b) + E_{ij}^{(2)}(-a, -b) - E_{ij}^{(2)}(+a, -b) - E_{ij}^{(2)}(-a, +b)]/4$ which yields the general bilinear pseudospin model

$$\mathcal{H} = \sum_{\langle ij \rangle} \sum_{a,b=x,y,z} J_{ij}^{ab} e_i^a e_j^b. \quad (3)$$

For the TLAF geometry considered here, all bonds are centrosymmetric and the Co site has local D_{3d} symmetry, which forbids antisymmetric exchange and constrains J_{ij}^{ab} to four independent parameters. For a bond with in-plane angle ϕ_{ij} measured from the crystallographic **a**-axis, the symmetry constrains the bond angle dependence as [44–46]

$$[J_{ij}^{ab}] = \begin{pmatrix} J + 2J^{\text{PD}} \cos(\phi_{ij}) & -2J^{\text{PD}} \sin(\phi_{ij}) & -J^\Gamma \sin(\phi_{ij}) \\ -2J^{\text{PD}} \sin(\phi_{ij}) & J - 2J^{\text{PD}} \cos(\phi_{ij}) & J^\Gamma \cos(\phi_{ij}) \\ -J^\Gamma \sin(\phi_{ij}) & J^\Gamma \cos(\phi_{ij}) & \Delta J \end{pmatrix}. \quad (4)$$

Here, for example, the bond along crystal **b**-axis corresponds to $\phi_{ij} = 2\pi/3$ [see a green dashed arrow in Fig. 1(c)]. The bond angle dependence arises solely from J^{PD} and J^Γ . The XXZ limit Eq. (1) is recovered for $J^{\text{PD}} = J^\Gamma = 0$. Our calculations show that these parameters are very small in the target materials. We therefore neglect these non-XXZ components in the following discussion. Such terms can nevertheless be important for bond dependent exchange parameters, such as those in the Kitaev model [47–49]. Although finite J^{PD} and J^Γ may prevent true superfluidity at zero-temperature, it has been shown that finite temperature can stabilize it [50, 51].

The nearest-neighbor (NN) exchange parameters of the X -site dependence for $X\text{BaCP}$ and $X\text{CSO}$ families are summarized in Fig. 2. Star points in the Fig. 2 indicate the experimental estimates of Δ (where available). In both families the interlayer exchange parameters are negligible, and further neighbor ones are also small (see Sec. S3 of SM for the full set of exchange parameters [35]). We therefore treat these compounds as effectively two-dimensional TLAFs. For NaBaCP and KCSO, our exchange parameters are in qualitative agreement with estimates from linear spin-wave fits [18, 28]. Notably, Δ differs strongly between $X\text{BaCP}$ and $X\text{CSO}$ families, and in both series Δ decreases systematically upon substituting X from Na to Cs. The calculated Δ already identifies several materials beyond NaBaCP and KCSO as super-solid candidates. At the same time, the $X\text{BaCP}$ series shows that X -site substitution can tune the XXZ model across the $\Delta = 1$ boundary, as KBaCP, RbBaCP, and CsBaCP move to the superfluid side.

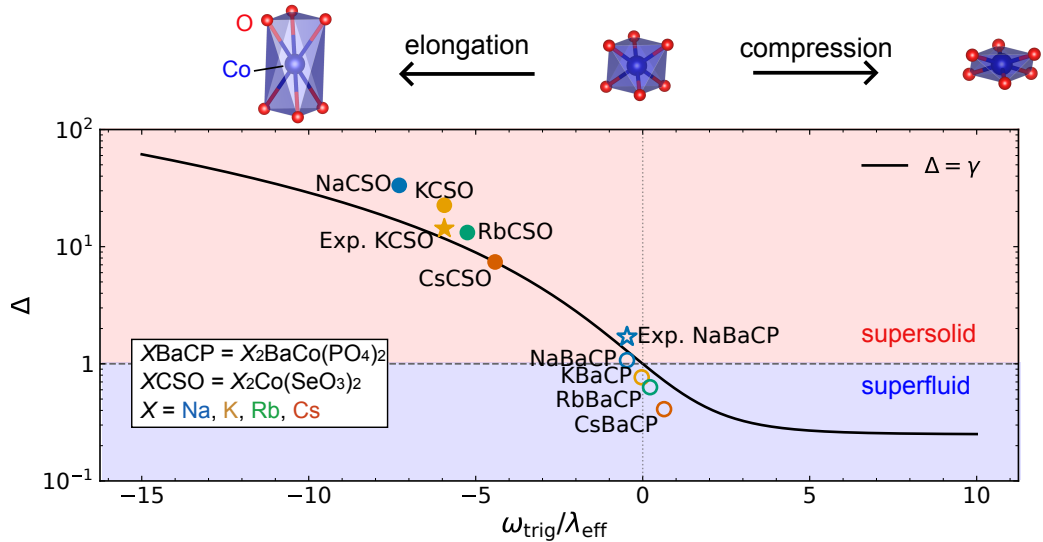


Figure 2. Plot of Δ as a function of $\omega_{\text{trig}}/\lambda_{\text{eff}}$ for the target materials. Solid and open circles denote calculated values for the XBaCP and XCSO series, respectively. While solid and open stars indicate experimental estimates for KCSO and NaBaCP , respectively. The solid black curve shows the theoretical relation $\Delta = \gamma$ as a function of $\omega_{\text{trig}}/\lambda_{\text{eff}}$ obtained by solving the minimal single-ion model in Eq. (5). Above the plot, schematic illustrations show the relation between the trigonal crystal field strength and the local CoO_6 distortion in a simplified picture that retains only the contribution of the surrounding O^{2-} ions.

Furthermore, Fig. 3 presents the map of Δ in the X - Y composition space in the XYCP family. Except for the already known NaBaCP member, the calculated compounds in the $\Delta > 1$ (red) region represent previously unexplored XYCP supersolid candidates. In particular, the Mg- and Ca-based XYCP families remain robustly on the supersolid for all X -site considered here. The Sr- and Ba-based families, by contrast, approach or cross the $\Delta = 1$ boundary depending on the X -site, demonstrating that the same mechanism can tune the system between the supersolid and superfluid. Similarly, Na-based NaYCP family also remains on the supersolid for all Y -site considered here.

$Y \backslash X$	Na	K	Rb	Cs
Mg	8.59	6.48	5.73	4.88
Ca	3.00	1.93	1.43	1.12
Sr	1.87	1.17	0.86	0.44
Ba	1.07	0.77	0.63	0.41

■ $\Delta > 1$: supersolid
■ $\Delta < 1$: superfluid

Figure 3. Δ in the XYCP family by combined X - and Y -site substitutions. The red and blue colors denote $\Delta > 1$ and $\Delta < 1$, respectively, corresponding to the supersolid and superfluid of the XXZ phase diagram.

To understand the microscopic origin of Δ , we first isolate the single-ion contributions to it in XYCP and XCSO . In an octahedral environment, the lowest-energy

term of high-spin Co^{2+} is ${}^4T_{1g}$ [52], which can be represented by an effective orbital moment $L_{\text{eff}} = 1$ coupled to $S = 3/2$. Atomic SOC splits this manifold into Kramers degenerate multiplets, with a $J_{\text{eff}} = 1/2$ Kramers doublet at the ground state [Fig. 1(b)]. The leading deviation from the octahedral symmetry allowed by the TLAFF local geometry is an axial trigonal crystal field. We thus consider the minimal single-ion Hamiltonian

$$\mathcal{H}_{\text{ion}} = \omega_{\text{trig}}[(L_{\text{eff}}^z)^2 - 2/3] + \lambda_{\text{eff}} \mathbf{L}_{\text{eff}} \cdot \mathbf{S}, \quad (5)$$

and note that J_z is conserved (since $[J_z, L_z^2] = 0$). Here the first term represents the trigonal crystal field (ω_{trig}) and the second term represents atomic SOC ($\lambda_{\text{eff}} > 0$). Diagonalizing this Hamiltonian, we find the ground state Kramers doublet as

$$|\psi_+\rangle = c_1|+1, -\frac{1}{2}\rangle + c_2|0, +\frac{1}{2}\rangle + c_3|-1, +\frac{3}{2}\rangle, \quad (6)$$

$$|\psi_-\rangle = \hat{T}|\psi_+\rangle, \quad (7)$$

in the $|L_{\text{eff}}^z, S^z\rangle$ basis, where \hat{T} is the time-reversal operator. In this basis the Hamiltonian can be chosen real, so we take c_1, c_2, c_3 to be real without loss of generality. We then introduce the spin projection factor s^a ($a = x, y, z$) for a generic Kramers doublet system (see Sec. S4 of the SM for details [35]). Within this doublet, the spin projection factors are [53, 54]

$$s^z = (-c_1^2 + c_2^2 + 3c_3^2)/2, \quad (8)$$

$$s^x = s^y = \left| \sqrt{3}c_1c_3 + c_2^2 \right| \equiv s^\perp. \quad (9)$$

We then define the single-ion anisotropy factor

$$\gamma \equiv \left(\frac{s^z}{s^\perp} \right)^2 = \left(\frac{-c_1^2 + c_2^2 + 3c_3^2}{2|\sqrt{3}c_1c_3 + c_2^2|} \right)^2. \quad (10)$$

γ becomes a universal function of a dimensionless ratio $\omega_{\text{trig}}/\lambda_{\text{eff}}$. For $\omega_{\text{trig}}/\lambda_{\text{eff}} = 0$, one recovers the cubic limit $s^x = s^y = s^z = 5/6$ and $\gamma = 1$. As $\omega_{\text{trig}}/\lambda_{\text{eff}} \rightarrow +\infty$, the doublet is dominated by the $|L_{\text{eff}}^z = 0\rangle$ component, giving $s^\perp = 1$, $s^z = 1/2$, and $\gamma \rightarrow 1/4$ (easy-plane). In contrast, as $\omega_{\text{trig}}/\lambda_{\text{eff}} \rightarrow -\infty$, the doublet approaches the $|L_{\text{eff}}^z = \pm 1\rangle$ sector, yielding $s^\perp \rightarrow 0$, $s^z \rightarrow 3/2$, and $\gamma \rightarrow \infty$ (easy-axis). A numerical evaluation yields the solid curve γ as a function of $\omega_{\text{trig}}/\lambda_{\text{eff}}$ in Fig. 2. For large positive $\omega_{\text{trig}}/\lambda_{\text{eff}}$, the gap ΔE_{ex} to the first excited doublet [Fig. 1 (b)] decreases. Therefore, the pseudospin-1/2 truncation is justified for $J \ll \Delta E_{\text{ex}}$. For XYCP and XCSO we find this truncation well satisfied (see Sec. S5 of SM [35]), validating the pseudospin-1/2 description. This establishes a direct link between the local Kramers doublet wavefunction and Δ as discussed in the followings.

We now discuss how the site parameter γ controls the bond anisotropy Δ governing emergence of the spin supersolid. We consider a total spin exchange tensor \mathcal{J}_{ij}^{ab} , acting within the ${}^4T_{1g}$ manifold of Co^{2+} in the absence of λ_{eff} and ω_{trig} [Fig. 1 (b)]. Upon including λ_{eff} and ω_{trig} and projecting onto the resulting Kramers doublet, one obtains the effective pseudospin-1/2 Hamiltonian in Eq. (3). This corresponds to the renormalization $J_{ij}^{ab} = s_i^a \mathcal{J}_{ij}^{ab} s_j^b$ (see Sec. S4 of SM [35]). Thus, the bond parameter Δ is controlled by the local single-site parameter γ through the projection factors s_i^a and s_j^b . Since there is only one distinct Co site per unit cell, these projection factors are site independent $s_i^a = s_j^a$, and it satisfies $\Delta \simeq \gamma$ [55]. The computed Δ for the XBaCP and XCSO families collapses almost onto the single-ion curve of γ as a function of $\omega_{\text{trig}}/\lambda_{\text{eff}}$ (Fig. 2). This limit then yields a symmetry-protected bound on the exchange anisotropy,

$$\Delta \geq \frac{1}{4}, \quad (11)$$

with $\Delta \rightarrow 1/4$ approached for $\omega_{\text{trig}}/\lambda_{\text{eff}} \rightarrow +\infty$ (see Fig. 2). Thus, the ideal XY limit ($\Delta \rightarrow 0$) is excluded, whereas the Ising limit ($\Delta \rightarrow \infty$) remains allowed.

The systematic evolution of Δ by the X - and Y - site substitution in the XYCP family and the X -site substitution in the XCSO family are driven predominantly by the O_6 contribution (Fig. 2). This indicates that X - and Y - site substitution acts mainly indirectly, by reshaping the local CoO_6 cage, rather than through the direct electrostatic contribution of the X - and Y -sites themselves. The structural origin of this oxygen-mediated tuning is the anisotropic lattice relaxation of the quasi-two-dimensional structure. Because the Co^{2+} ions form

a triangular network in the **ab** plane, the in-plane framework is more rigid than the interlayer direction, consistent with the negligible interlayer exchange couplings in XYCP and XCSO. As a result, chemical pressure is accommodated mainly by the **c**-axis response. For smaller cations, the relaxed structure exhibits a stronger **c**-axis distortion relative to the **ab** plane, which enhances the trigonal elongation of the local CoO_6 cage. In the convention of Eq. (5), this shifts ω_{trig} toward more negative values and therefore enhances Δ through the monotonic relation between Δ and γ . Larger cations produce the opposite structural response, shifting ω_{trig} upward and reducing Δ .

The point charge analysis reveals the origin of the large difference in the trigonal field strength between XBaCP and XCSO families as the cation environment (see Sec. S6 of SM [35]). In particular, the large negative trigonal field in XCSO is dominated by the nearby Se^{4+} ions. By contrast, in XBaCP the dominant oxygen and cation contributions partially cancel, yielding a much weaker net trigonal field.

In summary, we predict a previously unexplored set of supersolid candidates. We then show microscopically that the exchange anisotropy Δ in triangular-lattice Co^{2+} magnets is governed predominantly by the local trigonal crystal field through projection onto the Kramers doublet. This leads to a material independent relation $\Delta \simeq \gamma$ as a function of $\omega_{\text{trig}}/\lambda_{\text{eff}}$, with a symmetry protected bound $\Delta \geq 1/4$. This explains that the X - and Y -site substitution trends within each family is controlled predominantly by the O_6 ligands. On the other hand, our point charge analysis traces the large difference between the XYCP and XCSO families to the cation environment. These results establish trigonal field engineering as a microscopic design rule for realizing and tuning spin supersolidity in triangular-lattice magnets.

R. O. acknowledges insightful comments from Dr. Igor Solovyev. R. O. was supported by JSPS KAKENHI Grant No. JP23KJ2165. J. I. was supported by JSPS KAKENHI Grant No. JP24H00409. M. M. was supported by JSPS KAKENHI Grant No. JP23K03291 and GIMRT program (No. 202512-QBKNE-0013) of Quantum Beam Center for Materials Research, Institute for Materials Research, Tohoku University. S. M. was supported by JSPS KAKENHI Grant No. 24K00576.

-
- [1] H. Matsuda and T. Tsuneto, Off-Diagonal Long-Range Order in Solids, *Progress of Theoretical Physics Supplement* **46**, 411 (1970).
 - [2] K.-S. Liu and M. E. Fisher, Quantum lattice gas and the existence of a supersolid, *Journal of Low Temperature Physics* **10**, 655 (1973).
 - [3] S. Wessel and M. Troyer, Supersolid hard-core bosons on the triangular lattice, *Phys. Rev. Lett.* **95**, 127205 (2005).

- [4] D. Heidarian and K. Damle, Persistent supersolid phase of hard-core bosons on the triangular lattice, *Phys. Rev. Lett.* **95**, 127206 (2005).
- [5] R. G. Melko, A. Paramekanti, A. A. Burkov, A. Vishwanath, D. N. Sheng, and L. Balents, Supersolid order from disorder: Hard-core bosons on the triangular lattice, *Phys. Rev. Lett.* **95**, 127207 (2005).
- [6] M. Boninsegni and N. Prokof'ev, Supersolid Phase of Hard-Core Bosons on a Triangular Lattice, *Phys. Rev. Lett.* **95**, 237204 (2005).
- [7] D. Heidarian and A. Paramekanti, Supersolidity in the Triangular Lattice Spin-1/2 XXZ Model: A Variational Perspective, *Phys. Rev. Lett.* **104**, 015301 (2010).
- [8] D. Yamamoto, G. Marmorini, and I. Danshita, Quantum Phase Diagram of the Triangular-Lattice XXZ Model in a Magnetic Field, *Phys. Rev. Lett.* **112**, 127203 (2014).
- [9] Y. Huang, S. Yunoki, and S. Maekawa, Emergent Spin Supersolids in Frustrated Quantum Materials, *Advanced Materials* **n/a**, e00005.
- [10] J. Xiang, C. Zhang, Y. Gao, W. Schmidt, K. Schmalzl, C.-W. Wang, B. Li, N. Xi, X.-Y. Liu, H. Jin, G. Li, J. Shen, Z. Chen, Y. Qi, Y. Wan, W. Jin, W. Li, P. Sun, and G. Su, Giant magnetocaloric effect in spin supersolid candidate $\text{Na}_2\text{BaCo}(\text{PO}_4)_2$, *Nature* **625**, 270 (2024).
- [11] J. König, M. C. Bønsager, and A. H. MacDonald, Dissipationless spin transport in thin film ferromagnets, *Phys. Rev. Lett.* **87**, 187202 (2001).
- [12] S. Takei and Y. Tserkovnyak, Superfluid spin transport through easy-plane ferromagnetic insulators, *Phys. Rev. Lett.* **112**, 227201 (2014).
- [13] A. Qaiumzadeh, H. Skarsvåg, C. Holmqvist, and A. Brataas, Spin Superfluidity in Biaxial Antiferromagnetic Insulators, *Phys. Rev. Lett.* **118**, 137201 (2017).
- [14] Y. Gao, Y. Huang, S. Maekawa, and W. Li, Spin Seebeck Effect of Triangular Lattice Spin Supersolid, *Phys. Rev. Lett.* **135**, 236504 (2025).
- [15] M. Ulaga, J. Kokalj, T. Tohyama, and P. Prelovšek, The anisotropic Heisenberg model close to the Ising limit: triangular lattice vs. effective models (2025), [arXiv:2510.12667 \[cond-mat.str-el\]](https://arxiv.org/abs/2510.12667).
- [16] X. Xu, Z. Wu, Y. Chen, Q. Huang, Z. Hu, X. Shi, K. Du, S. Li, R. Bian, R. Yu, Y. Cui, H. Zhou, and W. Yu, NMR study of spin supersolid phases in the triangular-lattice antiferromagnet $\text{Na}_2\text{BaCo}(\text{PO}_4)_2$, *Phys. Rev. B* **112**, 125163 (2025).
- [17] M. Zhu, V. Romerio, N. Steiger, S. D. Nabi, N. Murai, S. Ohira-Kawamura, K. Y. Povarov, Y. Skourski, R. Sibille, L. Keller, Z. Yan, S. Gvasaliya, and A. Zheludev, Continuum excitations in a spin supersolid on a triangular lattice, *Phys. Rev. Lett.* **133**, 186704 (2024).
- [18] M. Zhu, L. M. Chinellato, V. Romerio, N. Murai, S. Ohira-Kawamura, C. Balz, Z. Yan, S. Gvasaliya, Y. Kato, C. D. Batista, and A. Zheludev, Wannier states and spin supersolid physics in the triangular antiferromagnet $\text{K}_2\text{Co}(\text{SeO}_3)_2$, *npj Quantum Materials* **10**, 74 (2025).
- [19] T. Chen, A. Ghasemi, J. Zhang, L. Shi, Z. Tagay, Y. Chen, L. Chen, E. S. Choi, M. Jaime, M. Lee, Y. Hao, H. Cao, B. L. Winn, A. A. Podlesnyak, D. M. Pajerowski, R. Zhong, X. Xu, N. P. Armitage, R. Cava, and C. Broholm, Phase diagram and spectroscopic signatures of a supersolid in the quantum Ising magnet $\text{K}_2\text{Co}(\text{SeO}_3)_2$, *Nature Communications* **10**, 1038/s41467-026-69661-0 (2026).
- [20] Y. Cui, Z. Wu, Z. Sun, K. Du, J. Luo, S. Li, J. Yang, J. Wang, R. Zhou, Q. Chen, Y. Kohama, A. Miyata, Z. Yang, R. Yu, and W. Yu, Spin-supersolidity induced quantum criticality and magnetocaloric effect in the triangular-lattice antiferromagnet $\text{Rb}_2\text{Co}(\text{SeO}_3)_2$ (2025), [arXiv:2509.26151 \[cond-mat.str-el\]](https://arxiv.org/abs/2509.26151).
- [21] K. Shi, Y. Q. Han, B. C. Yu, L. S. Ling, W. Tong, C. Y. Xi, T. Shang, Z. Wang, L. Pi, and L. Ma, Absence of high-field spin supersolid phase in $\text{Rb}_2\text{Co}(\text{SeO}_3)_2$ with a triangular lattice (2025), [arXiv:2509.06281 \[cond-mat.str-el\]](https://arxiv.org/abs/2509.06281).
- [22] R. Zhong, S. Guo, G. Xu, Z. Xu, and R. J. Cava, Strong quantum fluctuations in a quantum spin liquid candidate with a Co-based triangular lattice, *Proceedings of the National Academy of Sciences* **116**, 14505 (2019).
- [23] R. Zhong, S. Guo, and R. J. Cava, Frustrated magnetism in the layered triangular lattice materials $\text{K}_2\text{Co}(\text{SeO}_3)_2$ and $\text{Rb}_2\text{Co}(\text{SeO}_3)_2$, *Phys. Rev. Mater.* **4**, 084406 (2020).
- [24] N. Li, Q. Huang, X. Y. Yue, W. J. Chu, Q. Chen, E. S. Choi, X. Zhao, H. D. Zhou, and X. F. Sun, Possible itinerant excitations and quantum spin state transitions in the effective spin-1/2 triangular-lattice antiferromagnet $\text{Na}_2\text{BaCo}(\text{PO}_4)_2$, *Nature Communications* **11**, 4216 (2020).
- [25] T. Momoi and M. Suzuki, Ground-State Properties and Phase Diagram of the Quantum XXZ Antiferromagnet on a Triangular Lattice, *Journal of the Physical Society of Japan* **61**, 3732 (1992), <https://doi.org/10.1143/JPSJ.61.3732>.
- [26] D. Yamamoto, G. Marmorini, and I. Danshita, Microscopic Model Calculations for the Magnetization Process of Layered Triangular-Lattice Quantum Antiferromagnets, *Phys. Rev. Lett.* **114**, 027201 (2015).
- [27] D. Sellmann, X.-F. Zhang, and S. Eggert, Phase diagram of the antiferromagnetic XXZ model on the triangular lattice, *Phys. Rev. B* **91**, 081104 (2015).
- [28] J. Sheng, L. Wang, A. Candini, W. Jiang, L. Huang, B. Xi, J. Zhao, H. Ge, N. Zhao, Y. Fu, J. Ren, J. Yang, P. Miao, X. Tong, D. Yu, S. Wang, Q. Liu, M. Kofu, R. Mole, G. Biasiol, D. Yu, I. A. Zaliznyak, J.-W. Mei, and L. Wu, Two-dimensional quantum universality in the spin-1/2 triangular-lattice quantum antiferromagnet $\text{Na}_2\text{BaCo}(\text{PO}_4)_2$, *Proceedings of the National Academy of Sciences* **119**, e2211193119 (2022).
- [29] Y. Gao, Y.-C. Fan, H. Li, F. Yang, X.-T. Zeng, X.-L. Sheng, R. Zhong, Y. Qi, Y. Wan, and W. Li, Spin supersolidity in nearly ideal easy-axis triangular quantum antiferromagnet $\text{Na}_2\text{BaCo}(\text{PO}_4)_2$, *npj Quantum Materials* **7**, 89 (2022).
- [30] R. Zhong, S. Guo, G. Xu, Z. Xu, and R. J. Cava, Strong quantum fluctuations in a quantum spin liquid candidate with a Co-based triangular lattice, *Proceedings of the National Academy of Sciences* **116**, 14505 (2019), <https://www.pnas.org/doi/pdf/10.1073/pnas.1906483116>.
- [31] Y. Kajita, T. Nagai, S. Yamagishi, K. Kimura, M. Hagihara, and T. Kimura, Ferroaxial transitions in glaserite-type $\text{Na}_2\text{BaM}(\text{PO}_4)_2$ ($M = \text{Mg}, \text{Mn}, \text{Co}, \text{and Ni}$), *Chemistry of Materials* **36**, 7451 (2024).
- [32] M. Wildner, Isotypism of a selenite with a carbonate: Structure of the buetschliite-type compound $\text{K}_2\text{Co}(\text{SeO}_3)_2$, *Acta Crystallographica. Section C: Crystal Structure Communications* **48** (2025).
- [33] J. P. Perdew, K. Burke, and M. Ernzerhof, Generalized gradient approximation made simple, *Phys. Rev. Lett.*

- 77**, 3865 (1996).
- [34] P. Giannozzi, S. Baroni, N. Bonini, M. Calandra, R. Car, C. Cavazzoni, D. Ceresoli, G. L. Chiarotti, M. Cococcioni, I. Dabo, A. D. Corso, S. de Gironcoli, S. Fabris, G. Fratesi, R. Gebauer, U. Gerstmann, C. Gougoussis, A. Kokalj, M. Lazzeri, L. Martin-Samos, N. Marzari, F. Mauri, R. Mazzarello, S. Paolini, A. Pasquarello, L. Paulatto, C. Sbraccia, S. Scandolo, G. Sciauzero, A. P. Seitsonen, A. Smogunov, P. Umari, and R. M. Wentzcovitch, Quantum espresso: a modular and open-source software project for quantum simulations of materials, *Journal of Physics: Condensed Matter* **21**, 395502 (2009).
- [35] See Supplementary Material for details of calculations and extended discussions, including (S1) first-principles calculations and low energy Hubbard model, (S2) superexchange theory, (S3) exchange interactions further than nearest neighbor, (S4) single-ion spin-orbit entanglement in Kramers doublet (S5) validity of the Kramers-doublet (pseudospin-1/2) description, (S6) point charge crystal field analysis. The Supplementary Material includes Refs. [56–61].
- [36] N. Marzari and D. Vanderbilt, Maximally localized generalized wannier functions for composite energy bands, *Phys. Rev. B* **56**, 12847 (1997).
- [37] N. Marzari, A. A. Mostofi, J. R. Yates, I. Souza, and D. Vanderbilt, Maximally localized wannier functions: Theory and applications, *Rev. Mod. Phys.* **84**, 1419 (2012).
- [38] F. Aryasetiawan, K. Karlsson, O. Jepsen, and U. Schönberger, Calculations of Hubbard U from first-principles, *Phys. Rev. B* **74**, 125106 (2006).
- [39] P. W. Anderson, Antiferromagnetism. theory of superexchange interaction, *Phys. Rev.* **79**, 350 (1950).
- [40] I. V. Solovyev, Combining DFT and many-body methods to understand correlated materials, *Journal of Physics: Condensed Matter* **20**, 293201 (2008).
- [41] I. V. Solovyev, Superexchange interactions in orthorhombically distorted titanates RTiO_3 ($R=Y, \text{Gd}, \text{Sm}$ and La), *New Journal of Physics* **11**, 093003 (2009).
- [42] S. A. Nikolaev and I. V. Solovyev, Microscopic theory of electric polarization induced by skyrmionic order in GaV_4S_8 , *Phys. Rev. B* **99**, 100401 (2019).
- [43] R. Ono, S. Nikolaev, and I. Solovyev, Fingerprints of spin-current physics on magnetoelectric response in the spin- $\frac{1}{2}$ magnet $\text{Ba}_2\text{CuGe}_2\text{O}_7$, *Phys. Rev. B* **102**, 064422 (2020).
- [44] Y. Li, G. Chen, W. Tong, L. Pi, J. Liu, Z. Yang, X. Wang, and Q. Zhang, Rare-Earth Triangular Lattice Spin Liquid: A Single-Crystal Study of YbMgGaO_4 , *Phys. Rev. Lett.* **115**, 167203 (2015).
- [45] Y.-D. Li, X. Wang, and G. Chen, Anisotropic spin model of strong spin-orbit-coupled triangular antiferromagnets, *Phys. Rev. B* **94**, 035107 (2016).
- [46] Z. Zhu, P. A. Maksimov, S. R. White, and A. L. Chernyshev, Topography of spin liquids on a triangular lattice, *Phys. Rev. Lett.* **120**, 207203 (2018).
- [47] G. Jackeli and G. Khaliullin, Mott Insulators in the Strong Spin-Orbit Coupling Limit: From Heisenberg to a Quantum Compass and Kitaev Models, *Phys. Rev. Lett.* **102**, 017205 (2009).
- [48] J. G. Rau, E. K.-H. Lee, and H.-Y. Kee, Generic Spin Model for the Honeycomb Iridates beyond the Kitaev Limit, *Phys. Rev. Lett.* **112**, 077204 (2014).
- [49] S. M. Winter, A. A. Tsirlin, M. Daghofer, J. van den Brink, Y. Singh, P. Gegenwart, and R. Valentí, Models and materials for generalized Kitaev magnetism, *Journal of Physics: Condensed Matter* **29**, 493002 (2017).
- [50] J. V. José, L. P. Kadanoff, S. Kirkpatrick, and D. R. Nelson, Renormalization, vortices, and symmetry-breaking perturbations in the two-dimensional planar model, *Phys. Rev. B* **16**, 1217 (1977).
- [51] S. Park, S.-M. Park, Y.-T. Oh, H.-Y. Lee, and E.-G. Moon, Spin-orbit-induced instability and finite-temperature stabilization of a triangular-lattice super-solid (2026), arXiv:2601.20963 [cond-mat.str-el].
- [52] Y. Tanabe and S. Sugano, On the Absorption Spectra of Complex Ions, III The Calculation of the Crystalline Field Strength, *Journal of the Physical Society of Japan* **11**, 864 (1956).
- [53] T. Oguchi, Theory of Magnetism in $\text{CoCl}_2 \cdot 2\text{H}_2\text{O}$, *Journal of the Physical Society of Japan* **20**, 2236 (1965).
- [54] V. V. Men'shikov, V. V. Rudenko, V. I. Tugarinov, A. M. Vorotynov, and S. G. Ovchinnikov, Uniaxial magnetic anisotropy of rhombohedral CoCO_3 crystals at $T = 0$ K, *Physics of the Solid State* **56**, 468 (2014).
- [55] Difference between Δ and γ indicates effects from higher-order crystal field and anisotropic part of \mathcal{J}_{ij}^{ab} .
- [56] D. R. Hamann, Optimized norm-conserving Vanderbilt pseudopotentials, *Phys. Rev. B* **88**, 085117 (2013).
- [57] C. J. Ballhausen, *Introduction to Ligand Field Theory* (McGraw-Hill, New York, 1962).
- [58] A. Georges, L. d. Medici, and J. Mravlje, Strong Correlations from Hund's Coupling, *Annual Review of Condensed Matter Physics* **4**, 137 (2013).
- [59] T. Ribic, E. Assmann, A. Tóth, and K. Held, Cubic interaction parameters for t_{2g} Wannier orbitals, *Phys. Rev. B* **90**, 165105 (2014).
- [60] M. M. Ferreira-Carvalho, S. H. Chen, Y. C. Ku, A. Jose, R. Morrow, C. Y. Kuo, C. F. Chang, Z. Hu, M. W. Haverkort, and L. H. Tjeng, Direct evidence of a near-ideal $J_{\text{eff}} = 1/2$ ground state in triangular-lattice $\text{Na}_2\text{BaCo}(\text{PO}_4)_2$, *Phys. Rev. Mater.* **10**, 025004 (2026).
- [61] K. W. H. Stevens, Matrix Elements and Operator Equivalents Connected with the Magnetic Properties of Rare Earth Ions, *Proceedings of the Physical Society. Section A* **65**, 209 (1952).

Supplementary Materials: A microscopic design rule for spin supersolids in triangular-lattice magnets

Ryota Ono,¹ Jun'ichi Ieda,¹ Michiyasu Mori,¹ and Sadamichi Maekawa^{1,2}

¹*Advanced Science Research Center, Japan Atomic Energy Agency,
2-4 Shirakata, Tokai-mura, Ibaraki, 319-1195, Japan*

²*RIKEN Center for Emergent Matter Science (CEMS), Wako 351-0198, Japan*

S1 FIRST-PRINCIPLES CALCULATIONS AND LOW ENERGY HUBBARD MODEL

Electronic-structure calculations were performed using the plane-wave `Quantum ESPRESSO` package [1] with optimized norm-conserving pseudopotentials [2]. Spin-orbit coupling (SOC) is included at the level of fully relativistic pseudopotentials. We employ the Perdew–Burke–Ernzerhof exchange–correlation functional within the GGA [3].

In all compounds, the electronic structure near the Fermi level exhibits an isolated manifold of ten bands per Co site (five d orbitals \times two spin states), consistent with an ionic Co^{2+} picture. These bands predominantly originate from the Co^{2+} $3d$ orbitals. This motivates constructing a low-energy Hubbard model by realistic downfolding [4–6]. The corresponding 10 low-energy spin-orbitals are constructed using maximally localized Wannier functions implemented in `wannier90` [7, 8]. The screened on-site Coulomb interactions are evaluated by the constrained random phase approximation (cRPA) method [9].

The resulting low-energy effective model reads

$$\mathcal{H}^{\text{el}} = \mathcal{H}_{\text{one}} + \mathcal{H}_U \quad (\text{S1})$$

where \mathcal{H}_{one} is the one-electron term and \mathcal{H}_U is the on-site Coulomb interaction. The one-electron term is

$$\mathcal{H}_{\text{one}} = \sum_{ij} \sum_{ab} \sum_{\sigma\sigma'} h_{ij}^{ab;\sigma\sigma'} \hat{c}_{ia\sigma}^\dagger \hat{c}_{jb\sigma'}, \quad (\text{S2})$$

where $\hat{c}_{ia\sigma}^\dagger$ ($\hat{c}_{ia\sigma}$) creates (annihilates) an electron in orbital a with spin σ on site i . The on-site block ($i = j$) contains the crystal field and atomic SOC, while the intersite block ($i \neq j$) defines the hopping integrals $t_{ij}^{ab;\sigma\sigma'} \equiv h_{ij}^{ab;\sigma\sigma'}$.

The trigonal field splitting ω_{trig} is extracted from the on-site multiplet spectrum without including SOC. Within the ${}^4T_{1g}$ manifold, the trigonal crystal field splits the orbital triplet as $T_{1g} \rightarrow A_{2g} \oplus E_g$. In the effective $L_{\text{eff}} = 1$ representation, A_{2g} corresponds to $L_{\text{eff}}^z = 0$, while E_g corresponds to $L_{\text{eff}}^z = \pm 1$. Thus, we evaluate

$$\omega_{\text{trig}} = E({}^4E_g) - E({}^4A_{2g})$$

directly from the on-site splitting of the ${}^4T_{1g}$ multiplet.

We also extract the atomic SOC constant ζ_d by fitting the on-site SOC matrix to the one-electron form $\frac{\zeta_d}{2} \mathbf{l} \cdot \boldsymbol{\sigma}$ where \mathbf{l} is the orbital angular-momentum operator in the d -orbital basis and $\boldsymbol{\sigma}$ is the vector of Pauli matrices. For high-spin d^7 , the projection of the many-electron SOC operator $\frac{\zeta_d}{2} \sum_i \mathbf{l}_i \cdot \boldsymbol{\sigma}_i$ onto the parent 4F term gives $H_{\text{SOC}}^{(4F)} = \lambda_{\text{LS}} \mathbf{L} \cdot \mathbf{S}$, $\lambda_{\text{LS}} = -\frac{\zeta_d}{3}$, where \mathbf{L} is the true $L = 3$ orbital angular momentum. Within the cubic ${}^4T_{1g}$ component of the 4F term, the true orbital operator is related to the fictitious $L_{\text{eff}} = 1$ operator by $P_{T_{1g}} \mathbf{L} P_{T_{1g}} = -\frac{3}{2} \mathbf{L}_{\text{eff}}$ [10]. Therefore the SOC in the ${}^4T_{1g}$ manifold takes the form $H_{\text{SOC}}^{(4T_{1g})} = \lambda_{\text{eff}} \mathbf{L}_{\text{eff}} \cdot \mathbf{S}$ with $\lambda_{\text{eff}} = -\frac{3}{2} \lambda_{\text{LS}} = \frac{\zeta_d}{2}$. This equality holds in the pure ionic ${}^4T_{1g}({}^4F)$ limit.

The on-site Coulomb interaction $\mathcal{H}_U = \sum_i \mathcal{H}_{U,i}$ is parametrized by the spherical Kanamori form,

$$\mathcal{H}_{U,i} = U \sum_a \hat{n}_{ia\uparrow} \hat{n}_{ia\downarrow} + U' \sum_{a>b} \hat{n}_{ia} \hat{n}_{ib} - J_H \sum_{a>b} \sum_{\sigma\sigma'} \hat{c}_{ia\sigma}^\dagger \hat{c}_{ib\sigma'}^\dagger \hat{c}_{ia\sigma} \hat{c}_{ib\sigma'} + J_H \sum_{a>b} \left(\hat{c}_{ia\uparrow}^\dagger \hat{c}_{ia\downarrow}^\dagger \hat{c}_{ib\downarrow} \hat{c}_{ib\uparrow} + \text{h.c.} \right), \quad (\text{S3})$$

where $\hat{n}_{ia} = \sum_\sigma \hat{n}_{ia\sigma}$. All microscopic input parameters of the low-energy Hubbard model and the resulting NN spin-model parameters for $X_2\text{BaCo}(\text{PO}_4)_2$ ($X\text{BaCP}$) and $X_2\text{Co}(\text{SeO}_3)_2$ ($X\text{CSO}$) are summarized in Table S1. The corresponding results for $X_2Y\text{Co}(\text{PO}_4)_2$ ($XY\text{CP}$) are summarized in Table S2. The calculated Kanamori parameters are very similar across the compounds and satisfy the spherical-limit relation $U' = U - 2J_H$, as expected for $3d$ systems [11, 12].

S2 SUPEREXCHANGE THEORY

In our superexchange calculation we work in the local d^7 manifold of Co^{2+} . We construct the many-body basis in the $N = 7$ sector built from ten spin-orbitals, so that the local Hilbert-space dimension is $\binom{10}{7} = 120$ per site. To obtain the low-energy degrees of freedom, we diagonalize the on-site Hamiltonian: $\mathcal{H}_{\text{CF}} + \mathcal{H}_{\text{SOC}} + \mathcal{H}_{\text{U}}$ within the d^7 sector. The lowest-energy multiplet is a Kramers doublet $\{|\psi_{i+}\rangle, |\psi_{i-}\rangle\}$ at each site i . Next, within this doublet, we calculate maximal/minimal projection onto a pseudo-spin direction (e_i^x, e_i^y, e_i^z) . Using these basis states $\{|\pm e_i^a\rangle\}$ ($a = x, y, z$), we calculate the second-order perturbation energy given by:

$$E_{ij}^{(2)ab}(\mu, \nu) = \langle \mu e_i^a, \nu e_j^b | (\hat{T}_{ij} + \hat{T}_{ji}) | \mu e_i^a, \nu e_j^b \rangle, \quad (\text{S4})$$

where $\mu, \nu = \pm$, $|\mu e_i^a, \nu e_j^b\rangle = |\mu e_i^a\rangle \otimes |\nu e_j^b\rangle$ is a product state and \hat{T}_{ij} is a second-order perturbation operator:

$$\hat{T}_{ij} = - \sum_{\eta \in (d_i^8, d_j^6)} \frac{\hat{P}_{ij} \mathcal{H}_{\text{one},ji} |d_i^8, d_j^6; \eta\rangle \langle d_i^8, d_j^6; \eta| \mathcal{H}_{\text{one},ij} \hat{P}_{ij}}{E_{d_i^8, d_j^6; \eta} - E_0}. \quad (\text{S5})$$

Here $\{|d_i^8, d_j^6; \eta\rangle\}$ denotes a complete set of eigenstates in the virtual charge sector (d_i^8, d_j^6) with energies $E_{d_i^8, d_j^6; \eta}$. \hat{P}_{ij} is a projector excluding unphysical states. E_0 is the energy of the initial (d_i^7, d_j^7) state. Another virtual (d_i^6, d_j^8) sector is included in \hat{T}_{ji} . After obtaining the $E_{ij}^{(2)ab}(\mu, \nu)$, we can map onto an anisotropic exchange tensor by $J_{ij}^{ab} = (E_{ij}^{(2)ab}(+, +) + E_{ij}^{(2)ab}(-, -) - E_{ij}^{(2)ab}(+, -) - E_{ij}^{(2)ab}(-, +))/4$. Using these procedures, we obtain exchange parameters for all target compounds listed in Table S1.

Table S1. Microscopic input parameters of the low-energy Hubbard model and the resulting NN spin-model parameters for $X_2\text{BaCo}(\text{PO}_4)_2$ (XBaCP) and $X_2\text{Co}(\text{SeO}_3)_2$ (XCOS), $X = \text{Na}, \text{K}, \text{Rb}, \text{Cs}$. Values in parentheses are from experimental estimates [13–16]. We use the convention $\omega_{\text{trig}} = E(^4E_g) - E(^4A_{2g})$ and $\lambda_{\text{eff}} = \zeta_d/2$ for high-spin d^7 .

X	U (eV)	U' (eV)	J_H (eV)	ζ_d (meV)	ω_{trig} (meV)	$\omega_{\text{trig}}/\lambda_{\text{eff}}$	J (meV)	Δ	J^{PD} (meV)	J^{F} (meV)	γ
$X_2\text{BaCo}(\text{PO}_4)_2$ (XBaCP)											
Na	5.83	4.35	0.74	68 (66)	-16 (-11)	-0.47	0.132 (0.076)	1.1 (1.7)	-0.010	0.006	1.20
K	5.26	3.80	0.73	67	-1	-0.03	0.127	0.8	-0.009	-0.006	0.85
Rb	5.02	3.58	0.73	66	+7	+0.22	0.123	0.6	-0.009	-0.005	0.71
Cs	4.69	3.28	0.71	68	+22	+0.64	0.118	0.4	-0.010	-0.003	0.49
$X_2\text{Co}(\text{SeO}_3)_2$ (XCOS)											
Na	5.18	3.72	0.74	70	-255	-7.29	0.056	33.3	0.000	0.003	34.90
K	5.40	3.93	0.74	70	-208	-5.94	0.084 (0.217)	22.6 (14.3)	0.000	0.005	23.62
Rb	5.27	3.79	0.75	67	-176	-5.25	0.126	13.2	-0.001	0.007	13.70
Cs	5.18	3.70	0.74	66	-146	-4.42	0.203	7.4	-0.001	0.010	7.63

S3 EXCHANGE INTERACTIONS FURTHER THAN NEAREST-NEIGHBOR

In general, exchange interactions are not restricted to the nearest-neighbor (NN) bond. We therefore also examine further-neighbor couplings. Here J_2 and J_3 denote the second- and third-nearest-neighbor exchanges, respectively. In our structural geometry, the second-neighbor bond J_2 connects adjacent triangular layers and thus provides the leading interlayer coupling. This coupling is crucial for assessing whether a purely two-dimensional triangular-lattice antiferromagnet (TLAF) model is a good approximation. Table S3 summarizes the exchanges from J_2 (second NN) to J_3 (third NN). For simplicity, we show only the isotropic component, $J_n^{\text{iso}} \equiv \frac{1}{3} \sum_{a=x,y,z} J_n^{aa}$.

As shown in Table S3, the further-neighbor exchanges are substantially smaller than the NN interaction. For the XBACP family, $J_2/J_1 \simeq (0.1\text{--}0.25)\%$ and $J_3/J_1 \simeq (0.02\text{--}0.14)\%$. For the XCOS family, J_3 is negligible ($J_3/J_1 \lesssim 5 \times 10^{-4}$), while J_2 remains subdominant with $J_2/J_1 \leq 5.1\%$ (maximum at NaCSO). These results support a minimal TLAF description dominated by J_1 , with only weak corrections from further-neighbor couplings.

We also observe a systematic reduction of J_2 and J_3 upon substituting the X -site ion from Na to Cs. This is consistent with lattice expansion for larger X ions, which suppresses orbital overlap and hence superexchange.

Table S2. Microscopic input parameters of the low-energy Hubbard model and resulting NN spin-model parameters for $X_2Y\text{Co}(\text{PO}_4)_2$ ($XY\text{CP}$), with $X = \text{Na}, \text{K}, \text{Rb}, \text{Cs}$ and $Y = \text{Mg}, \text{Ca}, \text{Sr}, \text{Ba}$. We use $\omega_{\text{trig}} = E(^4E_g) - E(^4A_{2g})$ and $\lambda_{\text{eff}} = \zeta_d/2$ for high-spin d^7 . The Kanamori interaction parameters $U, U',$ and J_H are fixed to those of the corresponding parent $X\text{BaCP}$ compound.

X	Y	U (eV)	U' (eV)	J_H (eV)	ζ_d (meV)	ω_{trig} (meV)	$\omega_{\text{trig}}/\lambda_{\text{eff}}$	J (meV)	Δ	J^{PD} (meV)	J^Γ (meV)	γ
Na	Mg				67.2	-121.8	-3.62	0.033	8.60	0.001	-0.005	10.00
	Ca	5.83	4.35	0.74	67.8	-61.2	-1.81	0.077	3.00	0.003	0.007	3.34
	Sr				67.1	-41.1	-1.23	0.104	1.87	0.006	0.006	2.06
	Ba				68.2	-16.0	-0.47	0.132	1.07	0.010	0.006	1.19
K	Mg				66.4	-95.6	-2.88	0.034	6.49	0.001	-0.005	7.22
	Ca	5.26	3.80	0.73	67.0	-37.0	-1.10	0.080	1.93	0.004	-0.006	2.10
	Sr				66.4	-18.2	-0.55	0.105	1.17	0.007	-0.005	1.28
	Ba				67.2	-0.8	-0.02	0.127	0.77	0.009	-0.006	0.85
Rb	Mg				65.7	-92.0	-2.80	0.032	5.73	0.001	-0.005	6.15
	Ca	5.02	3.58	0.73	66.3	-24.4	-0.74	0.077	1.43	0.004	0.006	1.55
	Sr				65.7	-5.6	-0.17	0.099	0.86	0.007	-0.004	0.95
	Ba				66.8	6.6	0.20	0.122	0.63	0.009	-0.005	0.71
Cs	Mg				65.0	-67.2	-2.07	0.027	4.88	0.001	-0.005	5.16
	Ca	4.69	3.28	0.71	64.7	-12.1	-0.37	0.066	1.12	0.003	-0.006	1.21
	Sr				65.3	14.5	0.44	0.099	0.44	0.007	-0.004	0.53
	Ba				65.7	21.7	0.66	0.117	0.41	0.010	-0.003	0.49

Table S3. Isotropic exchange interactions J_n^{iso} (meV) for the NN (J_1^{iso}), second-NN (J_2^{iso}), and third-NN (J_3^{iso}) bonds.

X	J_1^{iso}	J_2^{iso}	J_3^{iso}
$X_2\text{BaCo}(\text{PO}_4)_2$ ($X\text{BaCP}$)			
Na	0.13516	0.00030	0.00019
K	0.11721	0.00029	0.00007
Rb	0.10761	0.00025	0.00006
Cs	0.09440	0.00010	0.00002
$X_2\text{Co}(\text{SeO}_3)_2$ ($X\text{CSO}$)			
Na	0.65972	0.03369	0.00010
K	0.68933	0.01097	0.00033
Rb	0.63592	0.00493	0.00008
Cs	0.63635	0.00154	0.00002

S4 SINGLE-ION SPIN-ORBIT ENTANGLEMENT IN KRAMERS DOUBLET

Let $\{|\psi_{i+}\rangle, |\psi_{i-}\rangle\}$ be the local ground state Kramers doublet on site i , obtained by diagonalizing the on-site Hamiltonian in many-body basis. Projecting the total spin operator S_i^a onto this doublet yields a 2×2 matrix,

$$\langle \psi_{is} | S_i^a | \psi_{is'} \rangle = \frac{1}{2} \sum_{\mu=x,y,z} \Lambda_i^{a\mu} (\sigma^\mu)_{ss'}, \quad (\text{S6})$$

$$s, s' = \pm, \quad a = x, y, z,$$

where σ^μ are the Pauli matrices in the $\{|\psi_{i+}\rangle, |\psi_{i-}\rangle\}$ basis. The real 3×3 matrix $\Lambda_i^{a\mu}$ encodes the single-ion spin-orbit entanglement. Then, the maximal projection along each pseudospin direction is given by $s_i^a \equiv \sqrt{\sum_{\mu=x,y,z} (\Lambda_i^{a\mu})^2}$. In the presence of local D_{3d} symmetry as in the case of $X\text{BaCP}$ and $X\text{CSO}$, one can choose the pseudospin axes such that $S_i^{x,y} = s_i^\perp e_i^{x,y}$ and $S_i^z = s_i^z e_i^z$, with $s_i^x = s_i^y \equiv s_i^\perp$.

S5 VALIDITY OF THE KRAMERS-DOUBLET (PSEUDOSPIN-1/2) DESCRIPTION

We evaluate the realistic splitting $\Delta E_{\text{ex}} = E_1 - E_0$ by exact diagonalization of the full on-site Hamiltonian $\mathcal{H}_{\text{CF}} + \mathcal{H}_{\text{SOC}} + \mathcal{H}_{\text{U}}$ in the local d^7 sector. Table S4 shows that $\Delta E_{\text{ex}} \simeq 20\text{--}32$ meV for all target materials, which is much larger than the exchange scale (of order meV or smaller). This confirms that the low-energy physics is well captured by the Kramers-doublet (pseudospin-1/2) description.

Table S4. Energy splitting between the ground state Kramers doublet (E_0) and a next lowest multiplet (E_1): $\Delta E_{\text{ex}} = E_1 - E_0$ in XBaCP and XCSO (meV). A value in parenthesis is an experimental splitting from X-ray absorption spectroscopy [16].

	NaBaCP	KBaCP	RbBaCP	CsBaCP	NaCSO	KCSO	RbCSO	CsCSO
ΔE_{ex}	29.93 (40)	31.56	29.19	23.52	20.07	20.45	19.50	19.88

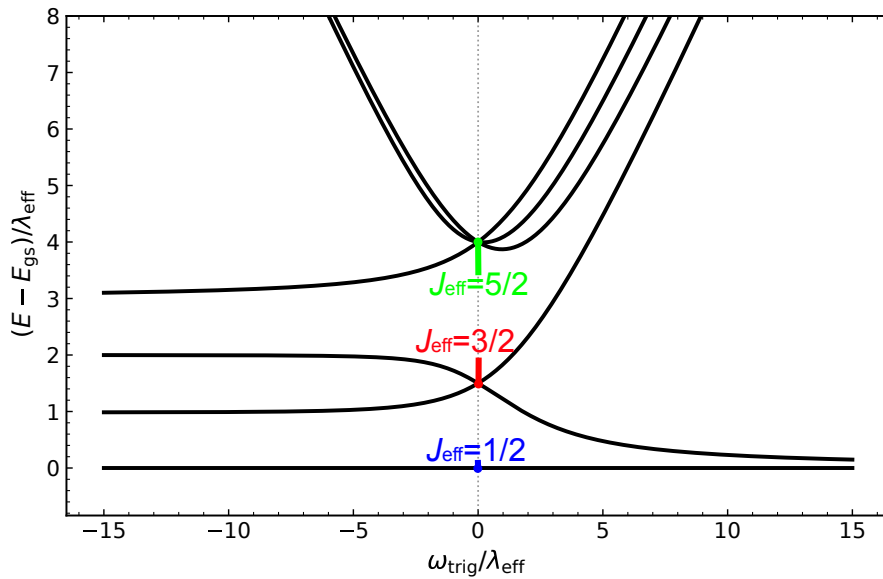


Figure S1. Energies of the two lowest Kramers doublets, measured relative to the ground-state energy, as a function of $\omega_{\text{trig}}/\lambda$. For $\omega_{\text{trig}} \neq 0$, J is not strictly conserved. The levels are therefore labelled by the dominant J_z character.

S6 POINT CHARGE CRYSTAL FIELD ANALYSIS

Here, we analyze the crystal field effect at Co^{2+} in XBaCP and XCSO families. We start from the point charge approximation for the electric potential at \mathbf{r} :

$$V(\mathbf{r}) = \sum_{\alpha} \frac{q_{\alpha}}{|\mathbf{R}_{\alpha} - \mathbf{r}|}, \quad (\text{S7})$$

where q_{α} is an effective ionic charge of ion α located at \mathbf{R}_{α} (with respect to the Co site taken as the origin).

For $|\mathbf{r}| \ll |\mathbf{R}_{\alpha}|$, the Coulomb kernel can be expanded in spherical harmonics as

$$\frac{1}{|\mathbf{R} - \mathbf{r}|} = \sum_{k=0}^{\infty} \sum_{q=-k}^k \frac{4\pi}{2k+1} \frac{r^k}{R^{k+1}} Y_{kq}(\Omega_{\mathbf{r}}) Y_{kq}^*(\Omega_{\mathbf{R}}), \quad (\text{S8})$$

where $\Omega_{\mathbf{r}}$ and $\Omega_{\mathbf{R}}$ denote the solid angles of \mathbf{r} and \mathbf{R} , respectively.

Choosing the local trigonal axis $\hat{\mathbf{n}}$ (defined from the local CoO_6 geometry), we focus on the axial ($q = 0$) components of the lattice potential. Their angular dependence can be decomposed with respect to Legendre polynomials as

$Y_{k0}(\Omega) \propto P_k(\cos \theta)$ with $\cos \theta = \hat{\mathbf{n}} \cdot \hat{\mathbf{R}}$. This motivates defining the axial multipole lattice sums

$$\mathcal{A}_{k0} \equiv \sum_{\alpha} q_{\alpha} \frac{P_k(\cos \theta_{\alpha})}{R_{\alpha}^{k+1}}, \quad \cos \theta_{\alpha} = \hat{\mathbf{n}} \cdot \hat{\mathbf{R}}_{\alpha}, \quad (\text{S9})$$

up to an overall prefactor common to all materials. Within the Stevens operator equivalent formalism [17], the axial crystal field parameters satisfy $B_k^0 \propto A_{k0} \langle r^k \rangle$, so \mathcal{A}_{k0} serves as a convenient geometric decomposition of the axial crystal field. For d electrons ($l = 2$), the leading nontrivial axial terms are $k = 2$ and $k = 4$ (the $k = 0$ term is a constant shift). Using $P_2(x) = (3x^2 - 1)/2$ and $P_4(x) = (35x^4 - 30x^2 + 3)/8$, we obtain

$$\mathcal{A}_{20} = \sum_{\alpha} q_{\alpha} \frac{P_2(\cos \theta_{\alpha})}{R_{\alpha}^3} = \frac{1}{2} \sum_{\alpha} q_{\alpha} \frac{3 \cos^2 \theta_{\alpha} - 1}{R_{\alpha}^3}, \quad (\text{S10})$$

$$\mathcal{A}_{40} = \sum_{\alpha} q_{\alpha} \frac{P_4(\cos \theta_{\alpha})}{R_{\alpha}^5} = \frac{1}{8} \sum_{\alpha} q_{\alpha} \frac{35 \cos^4 \theta_{\alpha} - 30 \cos^2 \theta_{\alpha} + 3}{R_{\alpha}^5}. \quad (\text{S11})$$

In practice, we use \mathcal{A}_{20} and \mathcal{A}_{40} as lattice sum descriptors to identify which coordination shells and chemical units dominantly generate the trigonal crystal field.

We define L as the side length of each O_3 triangle and d_z as the separation between the two O_3 triangle planes along the local trigonal axis, as shown in Fig. S3. We then introduce the dimensionless trigonal distortion parameter $r = \sqrt{3/2}(d_z/L)$. For an ideal octahedron, this definition gives $r = 1$. Thus, $r > 1$ corresponds to a trigonal elongation of the O_6 cage along the local trigonal axis, whereas $r < 1$ corresponds to a trigonal compression. This provides a simple local structural descriptor for the ligand contribution to the trigonal crystal field. However, r characterizes only the nearest-neighbor O_6 geometry and does not by itself determine the full crystal field, because the axial lattice sums \mathcal{A}_{20} and \mathcal{A}_{40} also contain contributions from more distant cations through their charges and distances. Therefore, in the following we use r to diagnose the local O_6 distortion, while \mathcal{A}_{20} and \mathcal{A}_{40} are used to decompose the total point charge crystal field into ligand and cation contributions.

The results of the axial multipole lattice sums for XBaCP and XCSeO are summarized in Fig. S4. The dominant contrast between the two families appears in the quadrupolar component \mathcal{A}_{20} . $|\mathcal{A}_{20}|$ is strongly suppressed in XBaCP , whereas it remains large and negative in XCSeO . This large difference mainly originates from the difference in the outer cation environment. In XCSeO , the outer environment contribution $\mathcal{A}_{20}^{\text{outer}}$ is sizeable and is dominated by the Se^{4+} units, yielding a large negative contribution that adds to the local O_6 component. In contrast, in XBaCP , the local O_6 contribution $\mathcal{A}_{20}^{\text{O}_6}$ is partially compensated by positive contributions from the surrounding cations, most notably Ba^{2+} , resulting in a near cancellation of the total \mathcal{A}_{20} . We also show the local environment around CoO_6 in NaBaCP and KCSO in Fig. S2. This tendency is captured by this local environment. In XCSeO , Se^{4+} is located almost in the triangular-lattice plane. In contrast, in XBaCP , P^{5+} and the X^+ sites are located above and below the triangular-lattice plane. This difference is crucial for the contrast between the cation contributions: $\mathcal{A}_{20}^{\text{P}}$ and $\mathcal{A}_{20}^{\text{Xsite}}$ in XBaCP , and $\mathcal{A}_{20}^{\text{Se}}$ in XCSeO .

Furthermore, upon increasing the alkali-metal ionic radius from Na to Cs, the magnitude of the local O_6 contributions systematically decreases. This systematic change is also reflected in the O_6 trigonal distortion parameter r (Table S5). This trend can be attributed to structural relaxation of the O_6 ligand cage. For smaller alkali-metal ions, the surrounding cage has more room to relax, which enhances the trigonal distortion of O_6 and results in a larger $|\mathcal{A}_{20}^{\text{O}_6}|$.

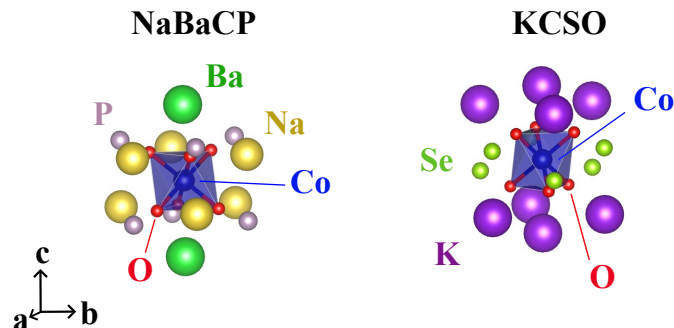


Figure S2. Local geometry around a CoO_6 cluster in NaBaCP and KCSO .

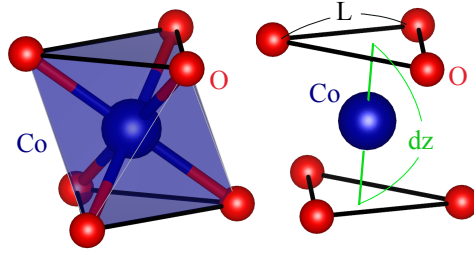


Figure S3. Local CoO_6 geometry. Crystallographic measures used to determine $r = \sqrt{3/2}(dz/L)$ are indicated as black solid lines and a green solid line, respectively.

	\mathcal{A}_{20}	$\mathcal{A}_{20}^{O_6}$	\mathcal{A}_{20}^{Xsite}	$\mathcal{A}_{20}^{P/Se}$	\mathcal{A}_{20}^{Ba}	\mathcal{A}_{40}	$\mathcal{A}_{40}^{O_6}$	\mathcal{A}_{40}^{outer}	
XBaCP	Na	-0.059	-0.076	-0.045	-0.049	+0.086	+0.119	+0.127	-0.007
	K	-0.079	-0.083	-0.042	-0.049	+0.077	+0.098	+0.104	-0.006
	Rb	-0.067	-0.073	-0.040	-0.051	+0.074	+0.092	+0.097	-0.006
	Cs	-0.017	-0.020	-0.026	-0.068	+0.065	+0.079	+0.085	-0.006
XCSO	Na	-0.347	-0.169	+0.056	-0.254	-	+0.131	+0.112	+0.019
	K	-0.326	-0.137	+0.044	-0.274	-	+0.130	+0.114	+0.017
	Rb	-0.300	-0.112	+0.040	-0.270	-	+0.117	+0.102	+0.015
	Cs	-0.269	-0.085	+0.033	-0.274	-	+0.110	+0.096	+0.013

Figure S4. Results of the point charge lattice sum analysis, using the definitions with Legendre prefactors P_2 and P_4 for XBaCP and XCSO. We list the axial multipole sums $\mathcal{A}_{20}, \mathcal{A}_{40}$ decomposed into the nearest O_6 and the outer environment, together with species resolved contributions to \mathcal{A}_{20} . For XBaCP we additionally list the Ba contribution to \mathcal{A}_{20} . Overall common prefactors are omitted. Color indicates the sign and magnitude of each contribution.

- [1] P. Giannozzi, S. Baroni, N. Bonini, M. Calandra, R. Car, C. Cavazzoni, D. Ceresoli, G. L. Chiarotti, M. Cococcioni, I. Dabo, A. D. Corso, S. de Gironcoli, S. Fabris, G. Fratesi, R. Gebauer, U. Gerstmann, C. Gougoussis, A. Kokalj, M. Lazzeri, L. Martin-Samos, N. Marzari, F. Mauri, R. Mazzarello, S. Paolini, A. Pasquarello, L. Paulatto, C. Sbraccia, S. Scandolo, G. Sclauzero, A. P. Seitsonen, A. Smogunov, P. Umari, and R. M. Wentzcovitch, Quantum espresso: a modular and open-source software project for quantum simulations of materials, *Journal of Physics: Condensed Matter* **21**, 395502 (2009).
- [2] D. R. Hamann, Optimized norm-conserving Vanderbilt pseudopotentials, *Phys. Rev. B* **88**, 085117 (2013).
- [3] J. P. Perdew, K. Burke, and M. Ernzerhof, Generalized gradient approximation made simple, *Phys. Rev. Lett.* **77**, 3865 (1996).
- [4] I. V. Solovyev, Combining DFT and many-body methods to understand correlated materials, *Journal of Physics: Condensed Matter* **20**, 293201 (2008).

Table S5. Trigonal distortion parameter r for XBaCP and XCSO. Experimental structural values are shown in parentheses, while the other values are obtained from theoretical structural relaxation.

X	XBaCP	XCSO
Na	(1.088)	1.220
K	1.109	(1.175)
Rb	1.099	1.150
Cs	1.030	1.116

- [5] S. A. Nikolaev and I. V. Solovyev, Microscopic theory of electric polarization induced by skyrmionic order in GaV_4S_8 , *Phys. Rev. B* **99**, 100401 (2019).
- [6] R. Ono, S. Nikolaev, and I. Solovyev, Fingerprints of spin-current physics on magnetoelectric response in the spin- $\frac{1}{2}$ magnet $\text{Ba}_2\text{CuGe}_2\text{O}_7$, *Phys. Rev. B* **102**, 064422 (2020).
- [7] N. Marzari and D. Vanderbilt, Maximally localized generalized Wannier functions for composite energy bands, *Phys. Rev. B* **56**, 12847 (1997).
- [8] N. Marzari, A. A. Mostofi, J. R. Yates, I. Souza, and D. Vanderbilt, Maximally localized Wannier functions: Theory and applications, *Rev. Mod. Phys.* **84**, 1419 (2012).
- [9] F. Aryasetiawan, K. Karlsson, O. Jepsen, and U. Schönberger, Calculations of Hubbard U from first-principles, *Phys. Rev. B* **74**, 125106 (2006).
- [10] C. J. Ballhausen, *Introduction to Ligand Field Theory* (McGraw-Hill, New York, 1962).
- [11] A. Georges, L. d. Medici, and J. Mravlje, Strong Correlations from Hund's Coupling, *Annual Review of Condensed Matter Physics* **4**, 137 (2013).
- [12] T. Ribic, E. Assmann, A. Tóth, and K. Held, Cubic interaction parameters for t_{2g} Wannier orbitals, *Phys. Rev. B* **90**, 165105 (2014).
- [13] J. Sheng, L. Wang, A. Candini, W. Jiang, L. Huang, B. Xi, J. Zhao, H. Ge, N. Zhao, Y. Fu, J. Ren, J. Yang, P. Miao, X. Tong, D. Yu, S. Wang, Q. Liu, M. Kofu, R. Mole, G. Biasiol, D. Yu, I. A. Zaliznyak, J.-W. Mei, and L. Wu, Two-dimensional quantum universality in the spin-1/2 triangular-lattice quantum antiferromagnet $\text{Na}_2\text{BaCo}(\text{PO}_4)_2$, *Proceedings of the National Academy of Sciences* **119**, e2211193119 (2022).
- [14] Y. Gao, Y.-C. Fan, H. Li, F. Yang, X.-T. Zeng, X.-L. Sheng, R. Zhong, Y. Qi, Y. Wan, and W. Li, Spin supersolidity in nearly ideal easy-axis triangular quantum antiferromagnet $\text{Na}_2\text{BaCo}(\text{PO}_4)_2$, *npj Quantum Materials* **7**, 89 (2022).
- [15] M. Zhu, L. M. Chinellato, V. Romerio, N. Murai, S. Ohira-Kawamura, C. Balz, Z. Yan, S. Gvasaliya, Y. Kato, C. D. Batista, and A. Zheludev, Wannier states and spin supersolid physics in the triangular antiferromagnet $\text{K}_2\text{Co}(\text{SeO}_3)_2$, *npj Quantum Materials* **10**, 74 (2025).
- [16] M. M. Ferreira-Carvalho, S. H. Chen, Y. C. Ku, A. Jose, R. Morrow, C. Y. Kuo, C. F. Chang, Z. Hu, M. W. Haverkort, and L. H. Tjeng, Direct evidence of a near-ideal $J_{\text{eff}} = 1/2$ ground state in triangular-lattice $\text{Na}_2\text{BaCo}(\text{PO}_4)_2$, *Phys. Rev. Mater.* **10**, 025004 (2026).
- [17] K. W. H. Stevens, Matrix Elements and Operator Equivalents Connected with the Magnetic Properties of Rare Earth Ions, *Proceedings of the Physical Society. Section A* **65**, 209 (1952).